

Strain-modulated superconductivity of monolayer Tc_2B_2

Zhengtao Liu(刘正涛), Zihan Zhang(张子涵), Hao Song(宋昊), Tian Cui(崔田) and Defang Duan(段德芳)

Citation: Chin. Phys. B, 2025, 34 (**4**): 047104. DOI: 10.1088/1674-1056/adb94d
Journal homepage: http://cpb.iphy.ac.cn; http://iopscience.iop.org/cpb

What follows is a list of articles you may be interested in

Two-dimensional Sb net generated nontrivial topological states in $SmAgSb_2$ probed by quantum oscillations

Jian Yuan(袁健), Xian-Biao Shi(石贤彪), Hong Du(杜红), Tian Li(李田), Chuan-Ying Xi(郗传英), Xia Wang(王霞), Wei Xia(夏威), Bao-Tian Wang(王保田), Rui-Dan Zhong(钟瑞丹), and Yan-Feng Guo(郭艳峰)
Chin. Phys. B, 2024, 33 (**7**): 077102. DOI: 10.1088/1674-1056/ad4bc2

Layered kagome compound $Na_2Ni_3S_4$ with topological flat band

Junyao Ye(叶君耀), Yihao Lin(林益浩), Haozhe Wang(王浩哲), Zhida Song(宋志达), Ji Feng(冯济), Weiwei Xie(谢韦伟), and Shuang Jia(贾爽)
Chin. Phys. B, 2024, 33 (**5**): 057103. DOI: 10.1088/1674-1056/ad3431

Spin direction dependent quantum anomalous Hall effect in two-dimensional ferromagnetic materials

Yu-Xian Yang(杨宇贤) and Chang-Wen Zhang(张昌文)
Chin. Phys. B, 2024, 33 (**4**): 047101. DOI: 10.1088/1674-1056/ad1380

Exciton-polaritons in a 2D hybrid organic-inorganic perovskite microcavity with the presence of optical Stark effect

Kenneth Coker, Chuyuan Zheng(郑楚媛), Joseph Roger Arhin, Kwame Opuni-Boachie Obour Agyekum, and Weili Zhang(张伟利)
Chin. Phys. B, 2024, 33 (**3**): 037102. DOI: 10.1088/1674-1056/ad1484

Effects of vacancy and external electric field on the electronic properties of the $MoSi_2N_4$/graphene heterostructure

Qian Liang(梁前), Xiangyan Luo(罗祥燕), Guolin Qian(钱国林), Yuanfan Wang(王远帆), Yongchao Liang(梁永超), and Quan Xie(谢泉)
Chin. Phys. B, 2024, 33 (**3**): 037101. DOI: 10.1088/1674-1056/acef04

RAPID COMMUNICATION

Strain-modulated superconductivity of monolayer Tc_2B_2

Zhengtao Liu(刘正涛)[1], Zihan Zhang(张子涵)[1], Hao Song(宋昊)[2], Tian Cui(崔田)[2,1], and Defang Duan(段德芳)[1,†]

[1] *Key Laboratory of Material Simulation Methods & Software of Ministry of Education, State Key Laboratory of Superhard Materials, College of Physics, Jilin University, Changchun* 130012, *China*

[2] *Institute of High Pressure Physics, School of Physical Science and Technology, Ningbo University, Ningbo* 315211, *China*

(Received 27 January 2025; revised manuscript received 10 February 2025; accepted manuscript online 24 February 2025)

Two-dimensional (2D) superconductors have attracted significant research interest due to their promising potential applications in optoelectronic and microelectronic devices. Herein, we employ first-principles calculations to predicted a new 2D conventional superconductor, Tc_2B_2, demonstrating its stable structural configuration. Remarkably, under biaxial strain, the superconducting transition temperature (T_c) of Tc_2B_2 demonstrates a significant enhancement, achieving 19.5 K under 3% compressive strain and 9.2 K under 11% tensile strain. Our study reveals that strain-induced modifications in Fermi surface topology significantly enhance the Fermi surface nesting effect, which amplifies electron–phonon coupling interactions and consequently elevates T_c. Additionally, the presence of the Lifshitz transition results in a more pronounced rise in T_c under compressive strain compared to tensile strain. These insights offer important theoretical guidance for designing 2D superconductors with high-T_c through strain modulation.

Keywords: two-dimensional, superconductivity, strain modulation, first-principles calculation

PACS: 71.15.Mb, 68.35.Gy, 74.25.Jb, 74.25.Kc

DOI: 10.1088/1674-1056/adb94d **CSTR:** 32038.14.CPB.adb94d

1. Introduction

Since the exfoliation of graphene from graphite in 2004,[1] researchers have recognized the possibility of synthesizing several atoms of thick two-dimensional (2D) materials. Given the underlying physical phenomena and applications brought about by their low dimension property,[2] 2D materials have been studied intensively in almost all fields of condensed matter physics, such as optoelectronics,[3,4] magnetism,[5] catalysis, batteries,[6] and superconductivity. As a result of the rapid development of experimental techniques in the last decade, such as twisting, carrier doping, chemical doping, and strain, several methods can be utilized to modulate 2D superconducting materials. Cao Yuan *et al.* twisted two graphene layers at a small angle to induce unconventional superconductivity in graphene similar to that of copper oxides.[7] Carrier doping via field-effect transistor gating enables the easy inducement of Ising superconductivity in transition-metal dichalcogenides.[8] The adsorption of hydrogen atoms to the surface increases the T_c of monolayer MgB_2 from 16 K to 65 K.[9]

The synthesis and application of 2D materials highly depend on the substrates used. An inevitable lattice mismatch exists between 2D materials and their substrates, and as a result, strain constantly exists in 2D materials in practice. Therefore, compared with other modulation methods, strain modulation is more fundamental for 2D materials. Moreover, strain regulation is more mature than other methods in terms of experimental technique, and numerous methods are available other than lattice mismatch, such as prestraining and bending of flexing substrates, heating or cooling and patterning substrates, and using piezoelectric substrates. Furthermore, atomic force microscopic tips and bubbles can also induce strain in 2D materials.[10] Therefore, it is crucial to systematically study the modulation mechanism of strain in the superconductivity of 2D materials.

In the study of 2D superconducting materials, relevant calculations are usually performed under biaxial strain to maintain the symmetry of crystal lattices. Hereafter, all "strain" mentioned in this study refers to "biaxial strain". Strain is defined as follows:

$$\varepsilon = \frac{l - l_0}{l}, \tag{1}$$

where l_0 indicates the freestanding lattice constant and l represents the lattice constant under strain. Thus, a zero strain means no strain is applied, a negative strain represents compressive strain, and a positive strain represents tensile strain.

Prompted by the successful discovery of MgB_2,[11] the discovery of new metal borides has been a resounding topic in the field of conventional superconductors until now.[12–17] In recent years, studies have theoretically predicted 2D metal borides that are modulated efficiently by strain. At -2% strain, the T_c of InB_6[18] and tetr-W_2B_2[19] increase from

†Corresponding author. E-mail: duandf@jlu.edu.cn

© 2025 Chinese Physical Society and IOP Publishing Ltd. All rights, including for text and data mining, AI training, and similar technologies, are reserved.

4.83 K to 19.23 K and from 7.8 K to 15.94 K, respectively; at 5% strain, the T_c of hydrogen monolayer MgB_2 shows an increase from 67 to 100;[9] at 11% strain, the T_c of AlB_6 increases from 4.7 K to 30 K;[20] and at −9% strain, the T_c of hydrogen monolayer Ti_2B_2 increases from 48.6 K to 69.4 K.[21] Although the effective modulation of strain on superconductivity has been reported, few studies have systematically investigated the effect of changes in the Fermi surface topology under strain on superconductivity.

NaCl-type structure is one of the most common structures in nature. To the best of our knowledge, only three compounds have been predicted to have a bilayer NaCl-type structure, namely, W_2B_2,[18] Mo_2B_2,[22] and Y_2S_2,[23] all of which are theoretically predicted to facilitate strain-modulated superconductivity. In this study, the swarm-intelligence-based structure prediction code (CALYPSO) was used to predict a new bilayer NaCl-type superconducting material,[24,25] Tc_2B_2, which can be stabilized between −3% and 11% strains. Such a high stability indicates the possibility of synthesizing Tc_2B_2 experimentally. Further calculations showed Tc_2B_2 as an intrinsic phonon-mediated superconductor with a T_c of 2.1 K. Interestingly, the T_c increased with strain and reached 19.5 K and 9.2 K at −3% and 11% strains, respectively. This remarkable enhancement in T_c is primarily attributed to the strengthening of the Fermi surface nesting (FSN) effect, driven by strain-induced modifications to the Fermi surface topology. Our findings provide theoretical guidance for the effective modulation of the superconductivity of conventional superconductors via strain modulation.

2. Computational methods

Structural optimizations and electron properties were calculated using the Vienna *Ab Initio* Simulation Package (VASP) code with projector-augmented wave pseudopotentials.[26] Perdew–Burke–Ernzerhof generalized gradient approximation was selected for the exchange–correlation functional.[27] To describe the possible van der Waals interactions in layered materials, we used the DFT-D2 method of Grimme in our calculations.[28] We prevented the nonphysical interaction among adjacent layers by setting the vacuum layers in all calculations to 20 Å. We adopted a cutoff energy of 800 eV and $0.02 \times 2\pi$/Å k-mesh density to achieve 10^{-6}-eV energy convergence for all calculations. The properties related to EPC were calculated using the QUANTUM ESPRESSO code.[29] Electron–ion interactions were described using ultrasoft pseudopotentials with a cutoff energy of 80 Ry (1 Ry = 13.6056923(12) eV). The self-consistent electron densities were calculated on a $28 \times 28 \times 1$ k-mesh with a Gaussian smearing of 0.04 Ry, and the dynamical matrices and EPC matrix elements were calculated on a $7 \times 7 \times 1$ q-mesh. We examined the thermal stability of Tc_2B_2 at temperatures of 300 K, 1000 K, 2000 K, and 2100 K by implementing *ab initio* molecular dynamics (AIMD) simulations in VASP code. All simulations lasted 5 ps in a $3 \times 3 \times 1$ supercell, using the NVT ensemble (canonical ensemble) to maintain a constant number of particles, volume, and temperature. To balance the calculation accuracy and calculation time, we considered a cutoff energy of 600 eV and a $2 \times 2 \times 1$ k-mesh in all AIMD calculations.

3. Results and discussion

3.1. Structure and stability

The Tc_2B_2 structure was predicted using warm intelligence-based CALYPSO code, which has been successfully used to predict a series of 2D materials with diverse structures and chemical compositions.[30] Tc_2B_2 has a $p4/nmm$ layer group, and its structure is shown in Fig. 1. Figure S1 in the supplementary materials displays the cell parameters, thickness d, intralayer, and interlayer Tc–B bond lengths. The freestanding case had a cell parameter of 2.99 Å, $d = 2.48$ Å, and intralayer and interlayer Tc–B bond lengths of 2.13 Å and 2.23 Å, respectively.

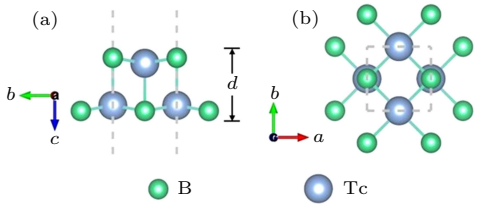


Fig. 1. (a) Side and (b) top views of the monolayer Tc_2B_2 structure.

To verify the energy stability of Tc_2B_2, we calculated its cohesive energy as follows:

$$E_{\text{coh}} = \frac{n_{\text{Tc}}E_{\text{Tc}} + n_{\text{B}}E_{\text{B}} - E_{\text{Tc}_2\text{B}_2}}{n_{\text{Tc}} + n_{\text{B}}}, \tag{2}$$

where n_{Tc} and n_{B} refer to the numbers of Tc and B atoms in a unit cell, respectively, and E_{Tc}, E_{B}, and $E_{\text{Tc}_2\text{B}_2}$ indicate the total energies of single isolated Tc atom, single isolated B atom, and one-unit-cell monolayer Tc_2B_2, respectively. The cohesive energy (E_{coh}) of Tc_2B_2 was 6.84 eV. Further, graphene, black phosphorene, and siliene had cohesive energies of 7.90 eV, 3.70 eV, and 4.04 eV, respectively.[31–33] The higher cohesive energy compared with that observed in these widely known 2D compounds suggests the high-stability energy of Tc_2B_2 and its potential for experimental synthesis.

According to the Born–Huang criteria, mechanical stability should satisfy the positive definite of an elastic modulus tensor. For 2D crystals, the following equation expresses the elastic modulus tensor in the standard Voigt notion scheme:

$$\begin{bmatrix} C_{11} & C_{12} & 0 \\ C_{21} & C_{22} & 0 \\ 0 & 0 & C_{66} \end{bmatrix}. \tag{3}$$

Thus, mechanically stable 2D crystals need to satisfy $C_{11}C_{22} - C_{12}^2 > 0$ and $C_{66} > 0$. Owing to the $p4/nmm$ symmetry of Tc_2B_2 $C_{11} = C_{22}$. Hence, Tc_2B_2 only needed to satisfy $C_{11} > |C_{12}|$ and $C_{66} > 0$. To guarantee the accuracy of our results, we adopted a $2 \times 2 \times 1$ supercell and a $12 \times 12 \times 1$ k-point mesh in the Brillouin zone during elastic modulus calculation. We obtained the following: $C_{11} = 231.71$ N/m, $C_{12} = 96.35$ N/m, and $C_{66} = 149.78$ N/m. Based on these results, we can conclude that the monolayer Tc_2B_2 is mechanically stable.

To further discuss the stability of Tc_2B_2 under strain, we calculated the phonon dispersion curves at -4% to 12% strains (Figs. 3(a)–3(c), S4, and S5). The absence of imaginary frequency in the phonons under -3% to 11% strains indicate the dynamic stability of Tc_2B_2 at this strain interval. Moreover, the stress–strain curve in Fig. S3 shows no downward trend and illustrates the mechanical stability of Tc_2B_2 at -3% to 11% strain intervals.

In addition, we examined the thermal stability of Tc_2B_2 at different temperatures via AIMD simulations. Figure S2 displays the snapshots, which reveal that Tc_2B_2 can retain a stable structure below 2100 K.

3.2. Phonon spectrum and isotropic superconductivity

Figure 2 displays the curves of T_c, electron–phonon coupling strength λ, and logarithmic average frequency ω_{log} as functions of strain, where T_c is calculated using the Allen–Dynes-modified McMillan equation with $\mu^* = 0.1$ (the equations for calculating T_c, λ, and ω_{log} are provided in the supplementary materials). The superconducting parameter of Tc_2B_2 changed considerably under strain. For the freestanding case, the T_c was only 2.1 K, owing to a small λ of 0.44. The T_c changed slowly under 0%–5% strains and accelerated from $\sim 6\%$ strain. As the strain increased to the limit strain of 11%, T_c increased to 9.2 K, with $\lambda = 0.94$ and $\omega_{log} = 146.0$ K. A -3% strain was applied, which caused an abnormally rapid increase in the T_c from 2.1 K to 19.5 K, with $\lambda = 1.43$ and $\omega_{log} = 176.0$ K. In the whole strain range, the λ and T_c curve showed the same U-shaped variation trend, whereas the variation trend of ω_{log} was an inverted U shape, which indicated that the superconductivity of Tc_2B_2 was dominated by the EPC strength. Therefore, the discussion in this study focuses on determining the physical essence of the enhancement in the EPC.

Based on the EPC-weighted phonon spectrums in Figs. 3(a)–3(c) and S4, several softening modes were observed in the acoustic branches under strain due to the improvement in the EPCs. At 3% strain, the softened phonons were almost imperceptible, and at 6% strain, acoustic branches near the X point softened. These modes softened further at 9% and 11% strains, which is consistent with the variation trend of λ in Fig. 2. At -3% strain, the acoustic branches softened along the Γ–M, M–X, and X–Γ paths, and the centers of these softening modes were roughly located at (2/3, 2/3), (1/3, 0), and (0, 2/3), respectively.

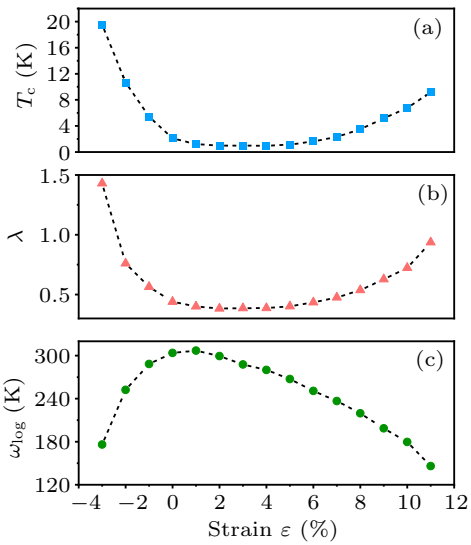


Fig. 2. (a) Curves of T_c, (b) electron–phonon coupling strength λ, (c) logarithmic average frequency ω_{log} as functions of strain.

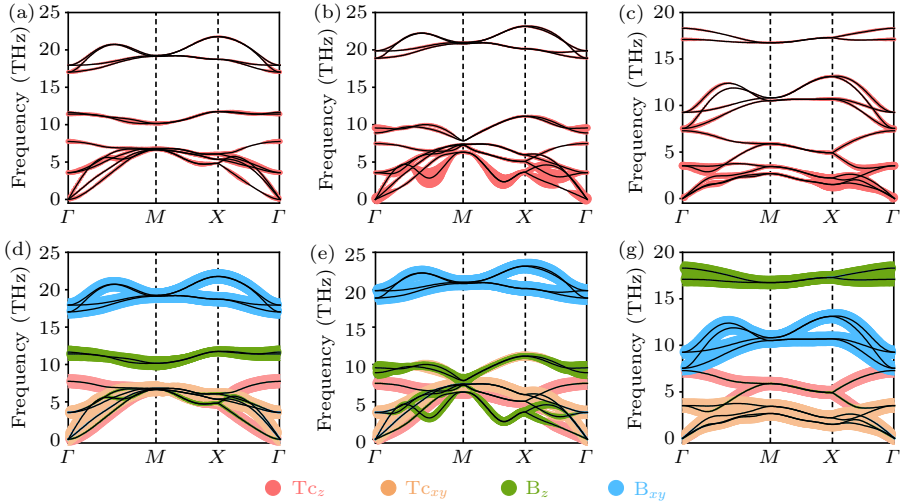


Fig. 3. Phonon spectrums weighted by EPC λ_{qv} (see Eq. (S3)) at (a) 0%, (b) -3%, and (c) 11% strains. Phonon spectrums weighted by the eigenvector modules of atom vibration modes at (d) 0%, (e) -3%, and (g) 11% strains.

Figures 3(d)–3(g) display the phonon spectrums weighted by the eigenvector modules of atom vibration modes at 0%, −3%, and 11% strains, which reflect the distribution of atomic vibration modes on phonon spectrums. For the freestanding case, the vibration modes of Tc atoms (in-plane mode Tc_{xy} and out-of-plane mode Tc_z) primarily populated the low-frequency region (below 8 THz). The out-of-plane modes of B atom B_z and in-plane modes of B atom B_{xy} dominated the middle- (10 THz–12 THz) and high-frequency regions (16 THz–22 THz), respectively. As displayed in Fig. S1, under compressive strain, the cell parameter decreased, and d increased, which further strengthened the overlap of atomic orbitals along the in-plane direction and weakened them along the out-of-plane direction. Thus, compressive strain strengthened the in-plane interactions and weakened the out-of-plane interactions among atoms. At −3% strain, this mechanism led to the appearance of the B_z mode in the low-frequency acoustic branches, where the softening modes were located. On the contrary, at 11% strain, the increase in cell parameters weakened the in-plane interactions and reduced the frequency of the Tc_{xy} mode. The Tc_{xy} mode almost single-handedly populated the low-frequency acoustic branches and contributed considerably to the total EPC.

3.3. Electron structure

Further, we calculated the electric energy bands at 0%, −3%, and 11% strains (Fig. 4). The positions of energy bands relative to the Fermi level changed visibly under strain due to electron transfer among various energy bands. Electron transfer occurred primarily among energy bands α, β, and γ, which were distinguished by blue, orange, and green colors along the Γ–M path, respectively. At 11% strain, the β band gained a number of electrons from the α band and went down to a deeper position. The α band almost no longer had electrons populating below the Fermi level. Under −3% strain, the α and β bands, especially the α band, gained electrons and moved down. Remarkably, the γ band lost electrons to form a new hole pocket at the Fermi level, and the Lifshitz transition occurred. Lifshitz transition refers to the change in Fermi surface connectivity without a broken symmetry;[34] this phenomenon can be induced by external parameters that exhibit continuous alterations, such as external electric/magnetic fields, doping, strain, or pressure.[35,36] Lifshitz transitions usually induce abrupt changes in material properties as well as in Tc_2B_2.

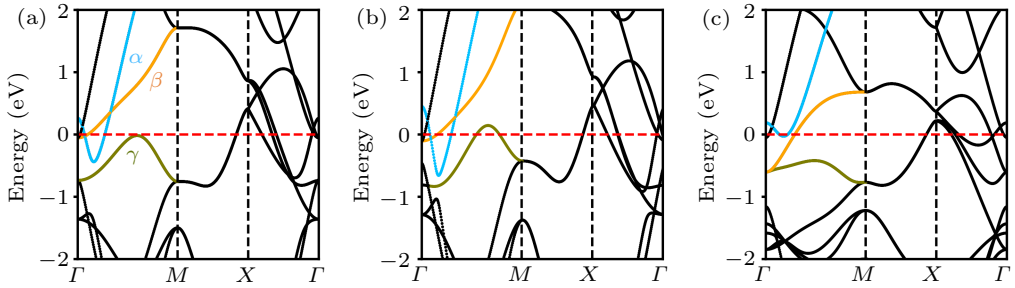


Fig. 4. Electric energy bands at (a) 0%, (b) −3%, and (c) 11% strains. Bands α, β, and γ are distinguished by blue, orange, and green lines, respectively. The Fermi levels of all energy bands were set to 0.

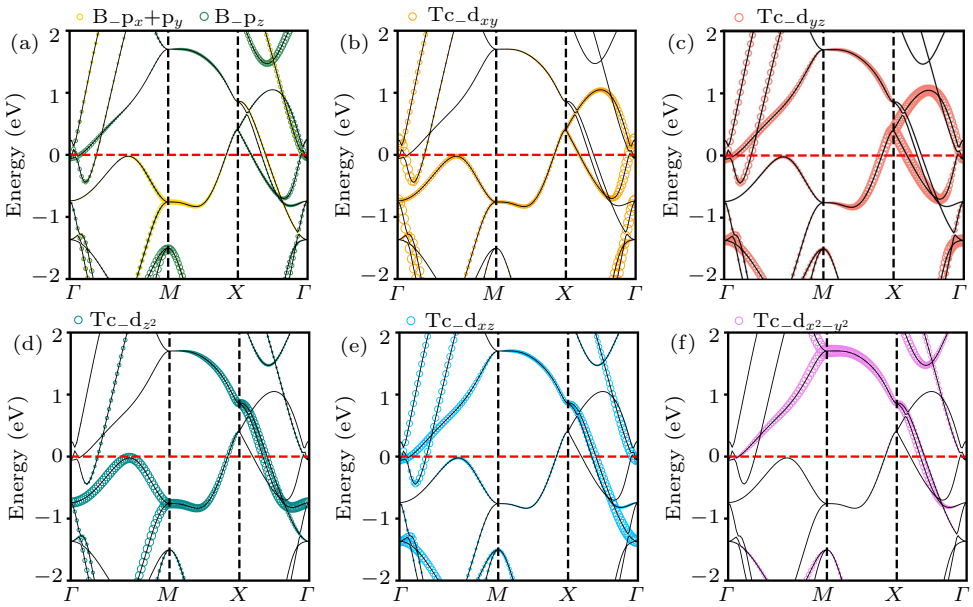


Fig. 5. Electric energy bands projected by (a) p_x plus p_y (green) and p_z (gold) orbitals of B, (b) d_{xy} (orange) orbital of Tc, (c) d_{yz} (red) orbital of Tc, (d) d_{z^2} (dark cyan) orbital of Tc, (e) d_{xz} (orange) orbital of Tc, and (f) $d_{x^2-y^2}$ (orange) orbital of Tc.

The overlap of atomic orbitals can be used to analyze the electron transfer among energy bands under strain.[37] Hence, we first determined the atom orbital populations of each band. Figure 5 shows the electric energy bands projected by various atom orbitals at 0% strain. As shown in Fig. 5, the α band was mainly populated by the p_x and p_y orbitals of B and d_{xy}, d_{yz}, and d_{xz} orbitals of Tc. The β band was mainly populated by the p_x and p_y orbitals of B and d_{yz}, d_{xz}, and $d_{x^2-y^2}$ orbitals of Tc. The γ band was mainly populated by the p_z orbital of B and d_{z^2} orbital of Tc. The atomic orbital and atomic space occupation are displayed in Fig. 1 using the same Cartesian coordinates. Based on the spatial orientation of atomic orbitals, we divided the orbital of Tc_2B_2 into three categories: (i) in-plane orbitals: p_x, p_y, d_{xy}, and $d_{x^2-y^2}$; (ii) out-of-plane orbitals: p_z and d_{z^2}; and (iii) d_{xz} and d_{yz} orbitals with in-plane and out-of-plane characteristics. Therefore, the majority of electrons in the α and β bands were contributed by in-plane orbitals, and most of the electrons in the γ band were contributed by out-of-plane orbitals. Compressive strain strengthened the overlap of in-plane orbitals and weakened the overlap of out-of-plane orbitals. The weakened overlap destabilized the γ band, and as a result, some electrons were transferred from the γ band to the α and β bands, which induced the Lifshitz transition.

3.4. Fermi surface nesting function and Fermi surface

To explore the causes of the EPC improvement of acoustic branch phonons, we used the ELK code to calculate the FSN functions (Fig. 6). The FSN function is defined as follows:

$$\xi(\boldsymbol{q}) = \frac{1}{N}\sum_{\boldsymbol{k},i,j}\delta(E_{\boldsymbol{k},i}-E_{\mathrm{F}})\,\delta(E_{\boldsymbol{k}+\boldsymbol{q},j}-E_{\mathrm{F}}), \tag{4}$$

where i and j denote the indices of different bands, $E_{\boldsymbol{k},\boldsymbol{q}}$ refers to the Kohn–Sham eigenvalue, E_{F} represents the Fermi energy, $\boldsymbol{q}$ represents the FSN vector, and N is the total number of k points in the first Brillouin zone. The value of ξ describes the probability that electrons $\boldsymbol{k}$ and $\boldsymbol{k}'$ on the Fermi surface are nested by $\boldsymbol{q}$. A special case that needs to be emphasized is that all FSN functions have their largest value at Γ point. However, $\xi(\boldsymbol{\Gamma})$ represents the Fermi surface nest with itself, which possesses no physical meaning. Based on Eq. (S3), the FSN function $\xi(\boldsymbol{q})$ is positively correlated with EPC $\lambda_{\boldsymbol{q}\nu}$ and plays a crucial role in determining the value of $\lambda_{\boldsymbol{q}\nu}$.

Based on the FSN function diagrams (Figs. 6(c) and 6(e)) under tensile strain, the FSN near point X gradually strengthened with the increase in strain, which is consistent with the increasing EPC of the phonon modes near the X point. The FSN function diagram at -3% strain in Fig. 6(b) shows two evident nonequivalent nestings strengthening, whose centers were approximately located at (2/3, 2/3) and (0, 2/3), which is consistent with the softening modes along the Γ–M and X–Γ paths.

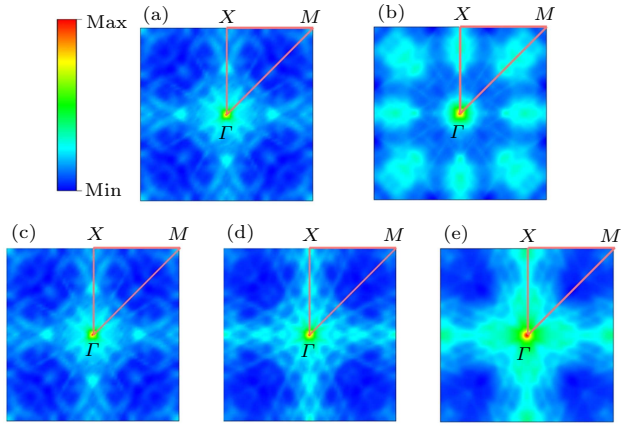


Fig. 6. FSN functions in the first Brillouin zone at (a) 0%, (b) −3%, (c) 6%, (d) 9%, and (e) 11% strains.

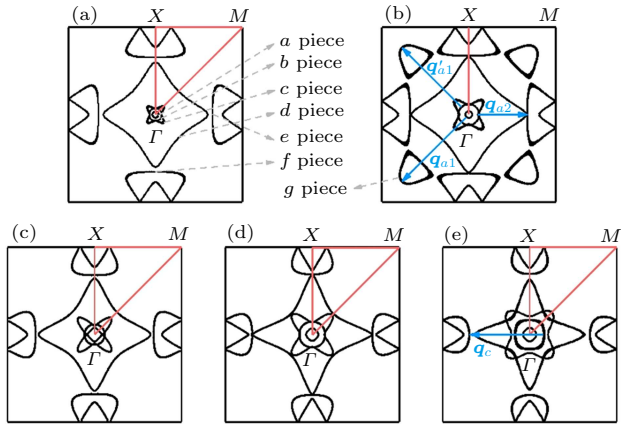


Fig. 7. Fermi surfaces at (a) 0%, (b) −3%, (c) 6%, (d) 9%, and (e) 11% strains. The blue arrows represent FSN vectors.

The definition of FSN $\xi(\boldsymbol{q})$ (Eq. (4)) shows that the FSN function is closely related to the Fermi surface topology. The FSN vector $\boldsymbol{q}$ can be identified directly from the Fermi surface. Fermi surface diagrams are shown in Fig. 7, letters *a*–*f* mark the six pieces of the Fermi surface from the center to the edge of the first Brillouin zone. The FSN effect under tensile strain involves two pieces of Fermi surface, namely, pieces *b* and *e*. The curvature of piece *b* along Γ–M decreased, and its circumference expanded with the increase in strain. In addition, the shape of piece *b* changed from a circle to a curved square. The shape of piece *e* can be approximated as a triangle with the top corner cut off, and the curvature of its bottom edge increased with increasing strain. In summary, given the co-deformation of pieces *b* and *e*, more parallel parts were observed between them, which means that the value of $\xi(\boldsymbol{q}_c)$ gradually increased. The $\boldsymbol{q}_{a2}$ vector exhibited a similar formation mechanism (Fig. 7(b)) to $\boldsymbol{q}_c$. At -3% strain, the adhesion area between piece *b* and the four-pointed star-shaped piece *c* increased, and piece *e* was nested by vector $\boldsymbol{q}_{a2}$. The FSN vector, $\boldsymbol{q}_{a2}$, induced the FSN near the (0, 2/3) point. The Lifshitz transition caused the appearance of four curved triangular hole pockets on the Fermi surface, which were denoted as piece *g*. The *g* piece nested pieces *a* and *b* with FSN vectors $\boldsymbol{q}_{a1}$ and

$\boldsymbol{q}'_{a1}$, respectively. As vector $\boldsymbol{q}_{a1}$ and $\boldsymbol{q}'_{a1}$ had the same direction, and their lengths were similar, they collectively induced the FSN near the (2/3, 2/3) point. Our discussion of FSN vectors will be further validated in the calculation of anisotropic superconductivity.

3.5. Anisotropic superconductivity

Given the anisotropy characteristics of 2D materials, we also calculated T_c using the anisotropic Migdal–Eliashberg theory based on the electron–phonon Wannier–Fourier interpolation in EPW.[38,39] A $100 \times 100 \times 1$ q-mesh and $200 \times 200 \times 1$ k-mesh were adopted to solve the Migdal–Eliashberg equations. To validate the accuracy of Wannier interpolation, figure S6 compares the energy bands calculated in both Bloch and Wannier representations under varying strains. Within the energy range of -2 eV to 2 eV, it is evident that the energy bands derived from the two representations are almost identical.

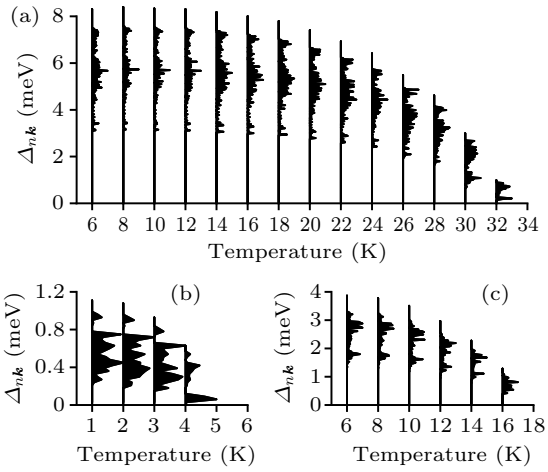


Fig. 8. Energy distribution of the superconducting energy gap, Δ_{nk}, as a function of temperature at (a) -3%, (b) 0%, and (c) 11% strains.

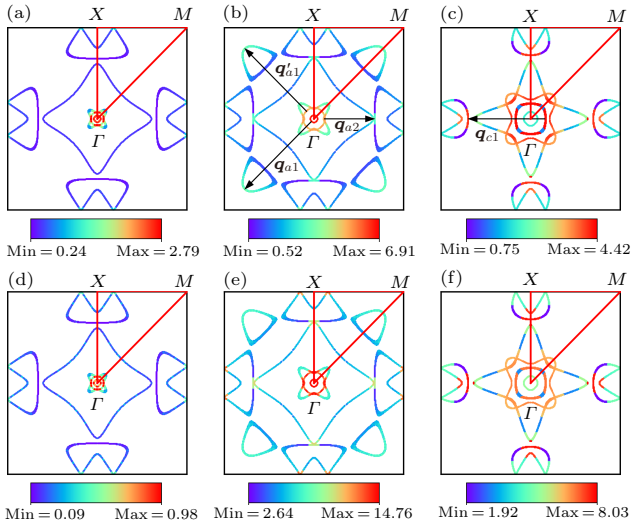


Fig. 9. Momentum-resolved EPC λ_{nk} at (a) 0%, (b) -3%, and (c) 11% strains. Momentum-resolved superconducting gap Δ_{nk} (meV) at (d) 0%, (e) -3%, and (f) 11% strains. At 0% strain, the Δ_{nk} was calculated at 2 K. At -3%, and 11% strains, the Δ_{nk} were calculated at 5 K.

Figure 8 shows the energy distribution of the superconducting energy gap Δ_{nk} as a function of temperature at various strains. At 0%, -3%, and 11% strains, the superconducting energy gap decayed to 0 at 4 K, 32 K, and 16 K, respectively. To verify the robustness of our discussion on FSN vectors in the chapter on FSN and Fermi surface, we calculated the momentum-resolved EPC λ_{nk} and superconducting gap Δ_{nk} (Fig. 9). Compared with the 0% strain case, at -3% strain, the λ_{nk} and Δ_{nk} of piece a increased by $\boldsymbol{q}_{a1}$, the λ_{nk} and Δ_{nk} of piece b increased by $\boldsymbol{q}'_{a1}$, and the λ_{nk} and Δ_{nk} of pieces c and e increased by $\boldsymbol{q}_{a2}$, at 11% strain, the λ_{nk} and Δ_{nk} of pieces b and e increased by $\boldsymbol{q}_c$. These λ_{nk} and Δ_{nk} increases further prove that the FSN effect contributed greatly to the enhancement of EPC and T_c of Tc_2B_2 under strain.

4. Conclusion

We predicted a new 2D superconducting material, Tc_2B_2, which can be stabilized between -3% and 11% strains. The high cohesiveness, dynamic lattice, and mechanical and thermal stability of Tc_2B_2 indicate its potential to be synthesized experimentally. The results of isotropic superconductivity calculations revealed that the T_c of Tc_2B_2 was 2.1 K for the freestanding case; however, it increased rapidly under strain. At -3% and 11% strains, the T_c reached 19.5 K and 9.2 K, respectively. Our study demonstrated that the T_c of Tc_2B_2 was dominated by EPC. The strengthening of the FSN effect, which was induced by modifications of the Fermi surface topology, greatly improved EPC under strain. Especially, the emergence of the Lifshitz transition significantly accelerated this process, resulting in a markedly faster enhancement of T_c under compressive strain compared to that under tensile strain. Our analysis of the Fermi surface topology effectively explained the T_c variation trend of Tc_2B_2 with strain and unveiled a microscopic mechanism underlying the strain-modulated conventional superconductivity in 2D materials. This study provides important guidance for the application of strain modulation in 2D conventional superconducting materials. Moreover, our work highlights the importance for researchers to not only focus on materials with intrinsic high-T_c, but also those with initially low-T_c that may achieve significant enhancements under strain modulation, especially in systems exhibiting Lifshitz transitions.

Acknowledgements

Project supported by the National Natural Science Foundation of China (Grant Nos. 12274169, 12122405, and 52072188), the National Key Research and Development Program of China (Grant No. 2022YFA1402304), the Program for Science and Technology Innovation Team in Zhejiang Province, China (Grant No. 2021R01004), and the Fundamental Research Funds for the Central Universities. Parts of calculations were performed in the High Performance Computing

Center (HPCC) of Jilin University and TianHe-1(A) at the National Supercomputer Center in Tianjin.

References

[1] Novoselov K S, Geim A K, Morozov S V, Jiang D, Zhang Y, Dubonos S V, Grigorieva I V and Firsov A A 2004 *Science* **306** 666

[2] Zhang H, Huang J X, Wang Y W, Liu R, Huai X L, Jiang J J and Anfuso C 2018 *Opt. Commun.* **406** 3

[3] Li H D, Luo T Y, Zhang S F, Sun Z J, He X, Zhang W F and Chang H X 2021 *Energy & Environ. Mater.* **4** 46

[4] Zhang X, Shao K, Yan C, Qin R, Lu Z, Geng H, Xu T and Ju L 2021 *Mater. Design* **200** 109452

[5] Jiang X, Liu Q, Xing J, Liu N, Guo Y, Liu Z and Zhao J 2021 *Appl. Phys. Rev.* **8** 109452

[6] Tao H, Fan Q, Ma T, Liu S, Gysling H, Texter J, Guo F and Sun Z 2020 *Prog. Mater. Sci.* **111** 100637

[7] Cao Y, Fatemi V, Fang S, Watanabe K, Taniguchi T, Kaxiras E and Jarillo-Herrero P 2018 *Nature* **556** 43

[8] Li W, Huang J, Li X, Zhao S, Lu J, Han Z V and Wang H 2021 *Mater. Today Phys.* **21** 100504

[9] Bekaert J, Petrov M, Aperis A, Oppeneer P M and Milošević M V 2019 *Phys. Rev. Lett.* **123** 077001

[10] Yang S X, Chen Y J and Jiang C B 2021 *Infomat.* **3** 397

[11] Nagamatsu J, Nakagawa N, Muranaka T, Zenitani Y and Akimitsu J 2001 *Nature* **410** 63

[12] Xie H, Wang H, Qin F, Han W, Wang S, Wang Y, Tian F and Duan D 2023 *Matter Radiat. Extrem.* **8** 058404

[13] Guo Z, Li X, Bergara A, Ding S, Zhang X and Yang G 2023 *Matter Radiat. Extrem.* **8** 068401

[14] Chen C H, Lan Y S, Huang A and Jeng H T 2024 *Nanoscale Horiz.* **9** 148

[15] Ma L, Wang L, Yuan Y, Guo H and Wang H 2023 *Chin. Phys. Lett.* **40** 086201

[16] Wang R, Sun Y, Zhang F, Zheng F, Fang Y, Wu S, Dong H, Wang C Z, Antropov V and Ho K M 2022 *Inorg. Chem.* **61** 18154

[17] Tao X, Yang A, Quan Y, Wan B, Yang S and Zhang P 2024 *Phys. Chem. Chem. Phys.* **26** 16963

[18] Yan L, Bo T, Liu P F, Zhou L J, Zhang J R, Tang M H, Xiao Y G and Wang B T 2020 *J. Mater. Chem. C* **8** 1704

[19] Yan L, Bo T, Zhang W X, Liu P F, Lu Z S, Xiao Y G, Tang M H and Wang B T 2019 *Phys. Chem. Chem. Phys.* **21** 15327

[20] Song B Y, Zhou Y, Yang H M, Liao J H, Yang L M, Yang X B and Ganz E 2019 *J. Am. Chem. Soc.* **141** 3630

[21] Han Y L, Li Y P, Yang L, Liu H D, Jiao D, Wang B T, Lu H Y and Zhang P 2023 *Mater. Today Phys.* **30** 100954

[22] Yan L, Bo T, Liu P F, Wang B T, Xiao Y G and Tang M H 2019 *J. Mater. Chem. C* **7** 2589

[23] Qu Z Y, Lin S Y, Xu M L, Hao J, Shi J M, Cui W W and Li Y W 2019 *J. Mater. Chem. C* **7** 11184

[24] Wang Y, Lv J, Zhu L and Ma Y 2012 *Comput. Phys. Commun.* **183** 2063

[25] Wang Y, Lv J, Zhu L and Ma Y 2010 *Phys. Rev. B* **82** 094116

[26] Kresse G and Furthmüller J 1996 *Phys. Rev. B* **54** 11169

[27] Perdew J P, Burke K and Ernzerhof M 1996 *Phys. Rev. Lett.* **77** 3865

[28] Grimme S 2006 *J. Comput. Chem.* **27** 1787

[29] Giannozzi P, Baroni S, Bonini N, Calandra M, Car R, Cavazzoni C, Ceresoli D, Chiarotti G L, Cococcioni M, Dabo I, Corso A Dal, de Gironcoli S, Fabris S, Fratesi G, Gebauer R, Gerstmann U, Gougoussis C, Kokalj A, Lazzeri M, Martin-Samos L, Marzari N, Mauri F, Mazzarello R, Paolini S, Pasquarello A, Paulatto L, Sbraccia C, Scandolo S, Sclauzero G, Seitsonen A P, Smogunov A, Umari P and Wentzcovitch R M 2009 *J. Phys.: Condens. Matter* **21** 395502

[30] Tang C, Kour G and Du A 2019 *Chin. Phys. B* **28** 107306

[31] Yang L M, Bačić V, Popov I A, Boldyrev A I, Heine T, Frauenheim T and Ganz E 2015 *J. Am. Chem. Soc.* **137** 2757

[32] Li L, Yu Y, Ye G J, Ge Q, Ou X, Wu H, Feng D, Chen X H and Zhang Y 2014 *Nat. Nanotechnol.* **9** 372

[33] Liu H, Neal A T, Zhu Z, Luo Z, Xu X, Tománek D and Ye P D 2014 *ACS Nano* **8** 4033

[34] Lifshitz I M 1960 *Sov. Phys. JETP* **11** 1130

[35] Aoki D, Seyfarth G, Pourret A, Gourgout A, McCollam A, Bruin J A N, Krupko Y and Sheikin I 2016 *Phys. Rev. Lett.* **116** 037202

[36] Liu C, Kondo T, Fernandes R M, Palczewski A D, Mun E D, Ni N, Thaler A N, Bostwick A, Rotenberg E, Schmalian, Bud'ko J S L, Canfield P C and Kaminski A 2010 *Nat. Phys.* **6** 419

[37] Zhai H C, Munoz F and Alexandrova A N 2019 *J. Mater. Chem. C* **7** 10700

[38] Noffsinger J, Giustino F, Malone B D, Park C H, Louie S G and Cohen M L 2010 *Comput. Phys. Commun.* **181** 2140

[39] Ponce S, Margine E, Verdi C and Giustino F 2016 *Comput. Phys. Commun.* **209** 116